# Laser discharge in a high-pressure jet of heavy noble gas: Expansion of emitting volume promises an efficient source of EUV light for lithography

I.S. Abramov,* S.V. Golubev, E.D. Gospodchikov, and A.G. Shalashov
*A. V. Gaponov-Grekhov Institute of Applied Physics of the Russian Academy of Sciences, Nizhny Novgorod, Russia*

A.A. Perekalov, A.N. Nechay, and N.I. Chkhalo
*Institute for Physics of Microstructures of the Russian Academy of Sciences, Nizhny Novgorod, Russia*

(Received 4 June 2024; revised 12 December 2024; accepted 9 January 2025; published 3 February 2025)

A discharge with multiply charged ions of a noble gas supported by a powerful infrared laser in a high-pressure jet is considered as a source of extreme ultraviolet (EUV) light radiation in particular narrow bands demanded by next-generation lithography. In a proof-of-principle experiment in krypton, the EUV-emitting region is visualized using a dedicated EUV microscope. Measurements support a basic model of underlying physics that involves expansion of the emitting plasma outside the laser focus. In simulations, we show that using the xenon jet, more optimal for EUV emission, may provide an efficiency competitive to the best commercial EUV sources for lithography.

DOI: 10.1103/PhysRevApplied.23.024004

## I. INTRODUCTION

Line radiation of multiply charged ions of xenon near 11-nm wavelength, where the spectra of these ions have a $4d$-$4f$ unresolved transition array (UTA) [1], has been recently proposed as a source of extreme ultraviolet (EUV) light for chip-production lithography [2]. Compared to early studies of xenon targets for EUV generation [3–6], there is major progress in the focusing of a narrow-band radiation at 11 nm based on multilayer Bragg structures, such as Ru/Be mirrors, which reflect over 70% of radiation at $11.2 \pm 1\%$ nm [7]. This defines a possible operation band for EUV light sources at $11.2 \pm 1\%$ nm; this band fits well the UTA emission peak of xenon located at 10–12 nm [8]. Recently, experiments on a laser discharge in high-pressure xenon jets demonstrated a high, up to 4%, conversion efficiency of the laser energy power to EUV light at $11.2 \pm 1\%$ nm [9–12], which is comparable to commercial EUV sources operating at $13.5 \pm 1\%$ nm [13–15]. Accompanying theoretical interpretation of these experiments reveals a crucial role of the discharge propagation outside the laser focus that increases the EUV emissivity [16]. Experimental data fit well to the model in which the EUV-emitting region expands due to fast photoionization of a surrounding gas and consecutive electron heating by a conductive thermal flux from a hot plasma spot inside the laser focus. This produces multiply charged and excited $Xe^{10+}$–$Xe^{12+}$ ions that emit efficiently at $11.2 \pm 1\%$ nm. Although it has not been observed yet, the simulations suggest that the EUV-emitting region must be several times larger compared to the laser focal spot of where the discharge is initiated.

In this paper, we present explicit experimental evidence of this phenomenon. The emitting region is visualized in space using a unique EUV microscope developed purposely for the present study. Measured EUV images validate our theoretical concept. Based on these results, we discuss the limiting parameters of the possible EUV light source for lithography based on a xenon jet. Here we refer to the Alpha-Machine, a cooperative project of the Institute for Physics of Microstructures of the Russian Academy of Sciences (IPM RAS) and A. V. Gaponov-Grekhov Institute of Applied Physics of the Russian Academy of Sciences (IAP RAS) aimed at the demonstration of an EUV lithographer operating at less than 13.5-nm wavelength [17]. This prototype machine is based on a discharge in xenon that, after optimization, has a potential to provide the conversion efficiency from laser to EUV light exceeding the record value reached in the available equipment for high-volume chip manufacturing.

## II. EXPERIMENTAL SETUP

Despite xenon ions having much better emissivity in the target EUV band, krypton is used for the first proof-of-principle experiment. It is more preferable for diagnostics of the emitting area as it allows for avoiding strong absorption of $11.2 \pm 1\%$ nm photons due to photoionization of a residual gas, the case typical for xenon [18]. In this band, krypton has a much smaller photoionization cross section

*Contact author: abramov@ipfran.ru

 

compared to xenon—for gas densities used in our experiment, the mean free path of the 11.25-nm photon is 40 μm in xenon and 600 μm in krypton. The latter is comparable to a gas-jet radius, thus the target EUV radiation of krypton plasma reaches the detector without severe distortion, which facilitates the imaging of the EUV-emitting zone at that particular band. However, most of the radiation power of krypton ions falls in a wavelength range near the local maximum of the photoionization cross section at 6–8 nm [19]. In this band, the photoionization is 3 times more intense than at $11.2 \pm 1\%$ nm. The photon mean free path characterizing the overall emission of multiply charged krypton ions is about 200 μm, the value smaller than the gas-jet radius. Thus, the expansion of the emitting zone in krypton is driven by out-of-band EUV photons with 6–8-nm wavelengths while in-band $11.2 \pm 1\%$-nm photons are poorly absorbed.

A schematic of the experiment is shown in Fig. 1. Neutral krypton enters the vacuum chamber trough the 5-mm-long conical supersonic nozzle with a critical diameter of 500 μm, a solution angle of 11°, and a pressure of 2–15 bar. The nozzle forms a slowly divergent axisymmetric gas jet with a radius of 550 μm in the emitting zone. To prevent overexposure of the detector, the experimental series is limited to the nozzle pressure from 2 to 6 bar. The initial neutral gas density in the emitting zone varies approximately proportional to the nozzle pressure from 0.5 to $1.6 \times 10^{19}$ cm$^{-3}$. The discharge is supported by the Nd:YAG laser with 1.064-μm wavelength, 0.2-J energy per pulse, 10-ns pulse duration, and 2-Hz pulse repetition. Laser radiation is focused on a gas target by a short-focus lens with a focal length of 45 mm. Diameter of the focal waist is 66 μm, and the Rayleigh length is 300 μm. The whole focusing tract, including lens, input window, prism, and dividing plate, transmits 80% of input laser power, thus 0.16 J of the pulse energy reach the focal area. The laser beam is focused at the jet axis $x$ at 0.5 mm from the nozzle output and propagates along axis $y$, as shown in Fig. 1. At the focal spot, the laser radiation causes gas breakdown and formation of plasma with multiply charged ions emitting EUV light.

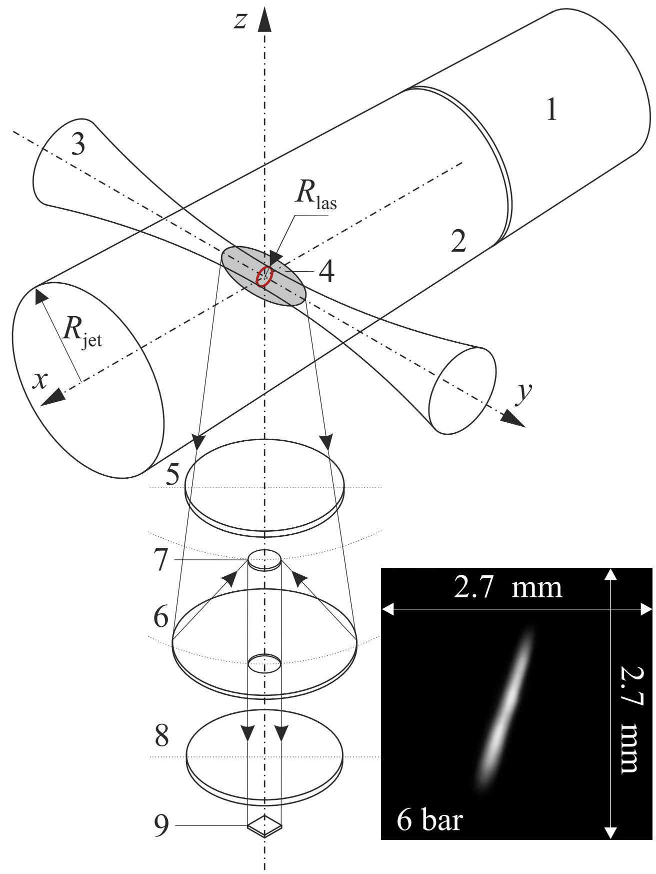


FIG. 1. Schematic of the experiment: 1, supersonic conical nozzle; 2, gas jet; 3, laser beam; 4, EUV-emitting plasma; 5 and 8, Mo/Be thin-film filters; 6, concave Mo/Be mirror; 7, convex Mo/Be mirror; 9, matrix detector. The jet radius ($R_{jet}$) and the radius of the focal waist ($R_{las}$) are indicated. Inset: sample image of the EUV-emitting region in krypton jet at 6-bar nozzle pressure.

EUV radiation is collected with a microscope, see Fig. 1. This diagnostic tool is made possible with Mo/Be multilayer optics developed by the authors particularly for the present study. The radiation passes through a multilayer thin-film filter based on the Mo/Be structure suppressing long-wave radiation with $\lambda > 20$ nm [20]. Then the radiation is focused with Schwarzschild's dual reflector consisting of concave and convex Mo/Be multilayer mirrors with near 70% peak reflectivity at 11.25 nm [21]. Thus, the reflector forms a beam of EUV light of $11.25 \pm 0.08$ nm wavelength band determined as a half-maximum of the total transmission of the two-mirror system. Passing the second Mo/Be thin-film filter that cut remaining long-wave noise, the EUV light comes to a two-coordinate back-side illuminated matrix detector GSENSE2020/BSI/PulSar (Gpixel) operating on CMOS technology. The PulSar technology allows elimination the antireflective coating on the sensor surface, significantly increasing sensitivity to EUV light [22]. The matrix has a sensitive zone of $13.3 \times 13.3$ mm$^2$ and a pixel array of $2048 \times 2048$. The pixel size is $6.5 \times 6.5$ μm$^2$, which, taking into account a five-fold magnification of the Schwarzschild's dual reflector, corresponds to 1.3 μm being projected to the discharge plane. Spatial resolution of an EUV microscope defined by reflector aberrations is approximately 3 pixels giving 3.9 μm in the discharge plane. A signal is accumulated in time during a single laser pulse. A sample raw image obtained with the microscope is shown in the inset of Fig. 1.

TABLE I. Width of the EUV region across the laser beam compared to its focal waist for different nozzle pressures.

| Nozzle pressure, bar | 2 | 3 | 4 | 6 |
|---|---|---|---|---|
| EUV $x$ size ($D4\sigma$), μm | 162 | 161 | 162 | 174 |
| EUV $x$ size (FWHM), μm | 98 | 98 | 101 | 106 |
| Laser waist ($D4\sigma$/FWHM), μm | | 66/39 | | |
| Theoretical estimate $D_{\mathrm{EUV}}$, μm | 101 | 102 | 100 | 95 |

## III. EXPERIMENTAL RESULTS

Figure 2 presents the results of postprocessing of the measured intensity maps of EUV emission in the $11.25 \pm 0.08$-nm band. Two-dimensional maps give the intensity distribution in the $(x, y)$ plane orthogonal to the microscope viewline, see Fig. 1. One-dimensional plots show distributions along the gas jet ($x$ axis) and the laser beam ($y$ axis). The most significant feature is an expansion of the EUV-emitting plasma transverse to the laser beam, which corresponds to the widening in $x$ direction. To make this statement quantitative, in Table I we list the $x$ sizes of the EUV-emitting region (at the focal waist) derived from the measured EUV maps as a quadruple root-mean-square ($D4\sigma$), i.e., a full-width at the $1/e^2$ level for an equivalent Gaussian distribution, and a FWHM. One can see that the emitting zone is considerably wider than the laser-beam waist and depends weakly on the gas pressure.

Note that at 6 bar, the detector matrix is close to saturation between the intensity peaks. This may result in increased dispersion of the EUV-intensity distribution along the $x$ axis due to an underestimated maximum in comparison to wings. At lower pressures, such an effect is absent.

## IV. BASIC PHYSICS

To proceed further, we need to recall the expanding discharge mechanism proposed in our early work [16].

Initially, the region of hot plasma occurs in the laser focal spot. After the breakdown, the electron temperature rapidly increases reaching 50–100 eV due to collisional absorption of the laser energy. Electron-impact step ionization causes the formation of highly charged ions with extremely high rates of spontaneous EUV emission, including but not limited to, the target band. After this, most of the absorbed power is spent on EUV radiation while the electron temperature drops to values well below 50 eV. The timescale of all these processes is approximately 100 ps.

Propagating outside the focal spot, the radiation of the highly charged ions creates a layer of secondary plasma due to photoionization of a gas surrounding the focal spot. This also happens on a fast timescale approximately 10 ps at which the ion motion is negligible. The "secondary" electrons gain energy due to thermal heat flux from the hot core (Spitzer conductivity); the temperature equilibration time is approximately 100 ps. The hot electrons produce and excite highly charged ions that emit EUV light just like the primary ions in the focal spot.

This process may be interpreted as an increase of the EUV emitting volume—the radial boundary of this volume moves with the velocity up to 100 μm/ns. At the end of the 10-ns laser pulse, the EUV-emitting plasma may be essentially larger than the initial volume constrained within the laser focus. Plasma expansion evolves at constant deposited laser power since the absorption takes place only inside the focus. Hence, the discharge slow evolution is accompanied by a decrease of the electron temperature and consequent variation of the ion-charge state distribution.

As the emission of EUV light in the target bands is strongly dependent on a particular composition of ion species, we show that this mechanism of plasma expansion plays a crucial role in its performance as an EUV light source [16].

## V. MULTIFLUID MODEL

To simulate the expanding discharge, we consider a model that consists of energy- and particle-balance equations describing the time evolution of the electron temperature $T_{\mathrm{e}}$, the ion temperature $T_{\mathrm{i}}$, the densities of unexcited $n_j$ and excited $n_j^*$ ion species, and equations for the characteristic linear dimensions of the hot-emitting plasma core, $R_{\mathrm{pl}}$, and of the whole discharge, $R_{\mathrm{pl}}^*$, including the outer layer of photoionized secondary plasma with the thickness $\Delta R = R_{\mathrm{pl}}^* - R_{\mathrm{pl}}$. The evolution of the linear dimension $R_{\mathrm{pl}}$ determines the evolution of the hot-plasma volume $V_{\mathrm{pl}}(t)$, over which the values $T_{\mathrm{e}}$, $T_{\mathrm{i}}$, $n_j$, and $n_j^*$ are averaged.

The equations of energy and particle balance in the hot-plasma core are formulated as

$$\frac{dn_j}{dt} = \sum_{s=1}^{8} b_{sj}, \quad \frac{dn_j^*}{dt} = \sum_{s=1}^{8} b_{sj}^*, \tag{1}$$

$$\frac{d}{dt}(V_{\mathrm{pl}} n_{\mathrm{e}} T_{\mathrm{e}}) = \sum_{s=1}^{8} a_s, \quad n\frac{d}{dt}(V_{\mathrm{pl}} T_{\mathrm{i}}) = -a_2. \tag{2}$$

Here $j = 1 \ldots j_{\max}$ enumerates the ion-charge states, $n_{\mathrm{e}}$ and $n$ are the electron and total ion densities satisfying the quasineutrality condition,

$$n_{\mathrm{e}} = \sum_{j=1}^{j_{\max}} Z_j (n_j + n_j^*), \quad n = \sum_{j=1}^{j_{\max}} (n_j + n_j^*). \tag{3}$$

The terms $a_s$, $b_{sj}$, $b_{sj}^*$ in the right-hand side of Eqs. (1)–(2) represent different channels defined in Table II and explained hereafter.

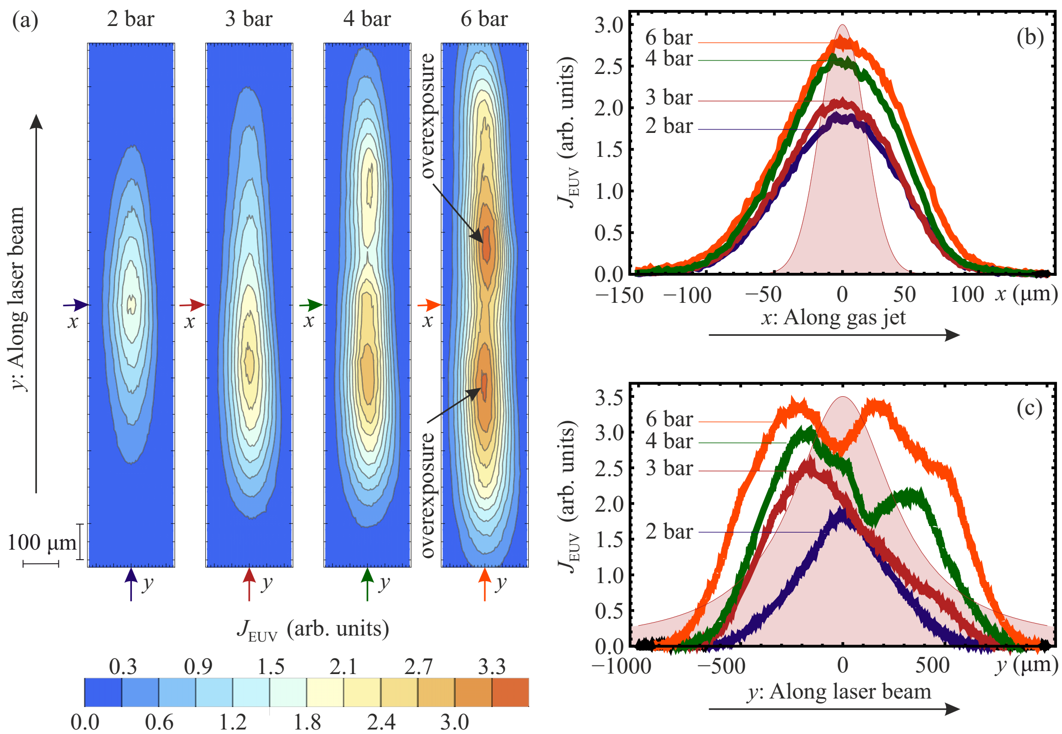


FIG. 2. Measured intensity of EUV emission at 11.25 ± 0.08 nm from krypton jet for the different nozzle pressures: contour plots of $J_{EUV}(x,y)$ (a), one-dimensional distributions along the gas jet, $J_{EUV}(x,0)$ (b), and along the laser beam, $J_{EUV}(0,y)$ (c). Pink shadows show corresponding distributions of the laser intensity. Cuts for the one-dimensional distributions are indicated by arrows of the same color in the two-dimensional contour plots.

The term $a_1$ describes the absorption of the laser radiation, which depends on the net rate of electron collisions, $\nu_e$, defined further, and the electron oscillatory energy

$$E_{osc} = 8\pi e^2 E_{las}/(m_e c\omega^2 t_{las}\pi R_{las}^2). \quad (4)$$

The rate $\nu_e$ defines what part of the energy $E_{osc}$ is converted to the electron temperature. Here $E_{las}$ is the energy of the laser-radiation pulse reaching the focal area, $t_{las}$ is the pulse duration, $\omega$ is the cyclic frequency of the laser radiation, $R_{las}$ is the radius of the focal waist, $e$ is the elementary charge, $m_e$ is the electron mass, and $c$ is the speed of light in vacuum.

Factor $\eta$ defines the attenuation of the laser intensity due to refraction of the laser beam,

$$\eta = 1 + \frac{\alpha R_{pl}^*}{2\Delta y}\mathrm{Ei}\left(-\frac{2(R_{pl}^*/R_{las})^2}{\cosh^2(\Delta y/\alpha R_{pl}^*)}\right), \quad \eta \in [0,1], \quad (5)$$

where $\Delta y$ is a discharge length along the laser beam, and Ei is the exponential integral function. This formula

TABLE II. Terms in balance Eqs. (1) and (2). Notations: $\Delta_m = 2m_e/m_i$ is the electron-ion energy exchange coefficient, $I_j$ are ionization energies of unexcited ions, $I_j^* = I_j - E_{ej}$ are ionization energies of excited ions, $\delta_{ij}$ is the Kronecker symbol.

| $s$ | | $a_s$ | $b_{sj}$ | $b_{sj}^*$ |
|---|---|---|---|---|
| 1 | Laser absorption [23] | $\eta\,\min[E_{osc}n_eV_0\ \nu_e\omega^2/(\omega^2+\nu_e^2),\ E_{las}/t_{las}]$ | 0 | 0 |
| 2 | Elastic collisions [23] | $-\Delta_m\sum_{j=1}^{j\max}k_{cj}(n_j+n_j^*)n_e(T_e-T_i)V_{pl}$ | 0 | 0 |
| 3 | Ionization [24,25] | $-\sum_{j=1}^{j\max}(I_jk_{ij}n_j+I_j^*k_{ij}^*n_j^*)n_eV_{pl}$ | $(k_{ij-1}n_{j-1}-k_{ij}n_j)n_e$ | $(k_{ij-1}^*n_{j-1}^*-k_{ij}^*n_j^*)n_e$ |
| 4 | Recombination [26] | $\sum_{j=2}^{j\max}(I_{j-1}^*n_j+(I_{j-1}^*+E_{ej})n_j^*)\alpha_{rj}n_e^2V_{pl}$ | $-\alpha_{rj}n_jn_e^2$ | $(\alpha_{rj+1}(n_{j+1}+n_{j+1}^*)-\alpha_{rj}n_j^*)n_e^2$ |
| 5 | Line excitation [27–32] | $\sum_{j=1}^{j\max}E_{ej}(k_{dj}n_j^*-k_{ej}n_j)n_eV_{pl}$ | $(k_{dj}n_j^*-k_{ej}n_j)n_e$ | $-(k_{dj}n_j^*-k_{ej}n_j)n_e$ |
| 6 | Line emission [27–33] | 0 | $A_j\theta_jn_j^*$ | $-A_j\theta_jn_j^*$ |
| 7 | Convective losses | $-n_eT_ec_aS_{pl}$ | $-n_jc_aS_{pl}/V_{pl}$ | $-n_j^*c_aS_{pl}/V_{pl}$ |
| 8 | Discharge expansion | 0 | $\nu_{exp}(\delta_{jZ^*}n_0-n_j)$ | $-\nu_{exp}n_j^*$ |

corresponds to refraction of geometric rays

$$r = r_0 \cosh\left(\frac{y}{\alpha R^*_{\rm pl}}\right), \quad \alpha = \sqrt{n_{\rm cr}/n_{\rm e} - 1} \tag{6}$$

in a "parabolic" medium with the electron-density variation across the laser beam $n_{\rm e}(r) = n_{\rm e}(0)\,[1 - (r/R^*_{\rm pl})^2]$; $n_{\rm cr}$ is the cutoff plasma density for laser radiation.

The terms with numbers $s = 2 \cdots 5$ describe elementary processes associated with the electron impact. Each term is proportional to a process-specific coefficient: $k_{{\rm c}j}$ for the elastic collisions, $k_{{\rm i}j}$ and $k^*_{{\rm i}j}$ for the ionization of unexcited and excited ions, $\alpha_{{\rm r}j}$ for the three-particle recombination, $k_{{\rm e}j}$ and $k_{{\rm d}j}$ for the excitation and deexcitation of ions, respectively. The coefficients are obtained by averaging of the cross sections of the corresponding process over Maxwell distribution assuming the essentially collisional plasma. Related sources of atomic data are listed in Table II. The net rate of electron collisions is then defined as follows:

$$\nu_{\rm e} = \sum_{j=1}^{j_{\max}}((k_{{\rm c}j} + k_{{\rm i}j} + k_{{\rm e}j} + \alpha_{{\rm r}j}n_{\rm e})n_j + \\ + (k_{{\rm c}j} + k^*_{{\rm i}j} + k_{{\rm d}j} + \alpha_{{\rm r}j}n_{\rm e})n^*_j). \tag{7}$$

The terms with $s = 6$ describe the line emission. Here we use the results of our previous research [16,32]. Only transitions from the ground state to excited electron configurations of an ion (and backward) are taken into account; almost all of the emission power is described in this way. For highly charged ions, these transitions have distinguished peaks in narrow bands of transition energies. Therefore, we combine all transitions of the $j$th ion in one with effective energy $E_{{\rm e}j}$ and net emission rate $A_j$ defined as

$$E_{{\rm e}j} = \sum_{l=1}^{l_{\max}} \alpha_{jl}A_{jl}E_{{\rm e}jl}/A_j\,, \qquad A_j = \sum_{l=1}^{l_{\max}} \alpha_{jl}A_{jl}. \tag{8}$$

Here $l = 1 \cdots l_{\max}$ enumerates the allowed transitions, $A_{jl}$ is the spontaneous emission rate of the $l$th transition of the $j$th ion, $E_{{\rm e}jl}$ is the energy of this transition, $\alpha_{jl}$ is the ratio of statistical weight of the ground level of this transition to total statistical weight of the ground electron configuration; see Ref. [32], Sec. III for further details.

Spontaneous emission rates in Table II are corrected with the probability $\theta_j(d)$ of the photon escaping, i.e., the probability to pass a distance of about $d = V_{\rm pl}/S_{\rm pl}$ towards the plasma boundary without reabsorption [33]. Here $S_{\rm pl}$ is the surface of core plasma volume $V_{\rm pl}$. In this way, we take into account the opacity of the inner plasma, which may significantly affect the performance of EUV light sources [34,35]. Typically, the probability $\theta_j(d)$ is about 5–10% for strong EUV lines for the case of interest.

The terms with $s = 7$ represent the convective losses associated with the escape of ion-electron pairs from the quasineutral core plasma volume with ion-acoustic velocity,

$$c_{\rm a} = \sqrt{\langle Z\rangle T_{\rm e}/m_{\rm i}}, \quad \langle Z\rangle = n_{\rm e}/n, \tag{9}$$

where $\langle Z\rangle$ is the average charge, $m_{\rm i}$ is the ion mass, and $\langle Z\rangle T_{\rm e} \gg T_{\rm i}$ is assumed.

The terms with $s = 8$ describe an additional source of cold particles due to the expansion of hot plasma volume with the rate $\nu_{\rm exp} = (V^{-1}_{\rm pl}\,dV_{\rm pl}/dt)_{R=R_{\rm pl}}$.

To close the model we need to define the size of the hot-plasma core $R_{\rm pl}$, and the outer size of the discharge $R^*_{\rm pl}$. The plasma core radius $R_{\rm pl}$ is defined from the following equation:

$$\frac{dR_{\rm pl}}{dt} = \frac{2\varkappa}{3n_{\rm e}\max(\Delta R, L_{\rm mfp})}. \tag{10}$$

Here $\Delta R = R^*_{\rm pl} - R_{\rm pl}$ is the thickness of the layer of the secondary photoionized plasma, $L_{\rm mfp}$ is the mean free path (mfp) of the photons with the energy $E_{\rm ph} = E_{{\rm e}j}$ defined from Eq. (8) with $j = Z$, where number $Z$ corresponds to the charge state of the ions that are dominating in the hot plasma and calculated as a floor function of the average charge, Eq. (9). Factor $\varkappa$ is the Spitzer-Braginskii coefficient of electron thermal conductivity in the heat-transfer equation for the electron temperature in completely ionized isotropic plasma [36,37]:

$$\frac{3}{2}n_{\rm e}\frac{\partial T_{\rm e}}{\partial t} = {\rm div}\,(\varkappa\nabla T_{\rm e})\,, \quad \varkappa = \frac{3\gamma_Z T_{\rm e}^{5/2}}{4\sqrt{2\pi m_{\rm e}}e^4\Lambda\langle Z\rangle}. \tag{11}$$

Here $\Lambda$ is the Coulomb logarithm, $\gamma_Z$ is the kinetic correction accounting for ion charge [38], $\gamma_Z \sim 10$ for cases with $\langle Z\rangle \sim 10$ considered hereafter. Equation (10) follows from the estimate $dR_{\rm pl}/dt = L_\varkappa/t_\varkappa$ where the spatial scale is an electron-temperature inhomogeneity scale assumed as $L_\varkappa = \max(\Delta R, L_{\rm mfp})$ and the temporal scale is taken Eq. (11) replacing the derivatives with $1/t_\varkappa$ and $1/L^2_\varkappa$. Note that the total line-radiation power from core plasma may be so high that the photon mean free path $L_{\rm mfp}$ is essentially shorter than the spatial scale $L_\varkappa$.

The time evolution of the outer discharge size $R^*_{\rm pl}$ is defined from the energy balance assuming that the neutral gas is ionized up to the maximum charge state $j = Z^*$ limited by the effective energy $E_{\rm ph}$ related to the photon mean free path in Eq. (10). The resulting equation is

$$\frac{dR^*_{\rm pl}}{dt} = \frac{P_{\rm rad}\;\Omega/4\pi}{n_0\sum_{j=0}^{Z^*-1}I_j}\left(\frac{dV_{\rm pl}}{dR}\right)^{-1}_{R=R^*_{\rm pl}}. \tag{12}$$

Here $P_{\rm rad}$ is the power of plasma radiation into $4\pi$ solid angle, $\Omega$ is the solid angle occupied by the neutral gas, $n_0$ is the neutral gas density in the focal waist vicinity, the sum represents the total energy cost of the $Z^*$th ion, $I_j$ is the ionization energy of the $j$th ion, $Z^*$ is the minimal $j$ satisfying condition $I_j > E_{\rm ph}$.

The dependence of the plasma volume on the linear size $V_{\rm pl}(R)$ is determined by the mutual location of the laser beam and the gas jet. Here we consider the plasma volume as an intersection of a cylinder jet with fixed radius $R_{\rm jet}$ and a cylinder coaxial to the laser beam but with evolving radius, $R_{\rm pl}$ for the hot plasma or $R^*_{\rm pl}$ for the cold plasma, and length. Ends of the latter cylinder expand with the same velocity as its radius.

Differential Eqs. (1), (2), (10), and (12) form a closed set. These equations are solved numerically. Initial conditions are as follows: completely ionized plasma is assumed, plasma density equals the density of neutral gas $n_0$, the electron temperature is of 3–5 eV (typical for a breakdown), the ion temperature is room temperature, and the core and outer plasma volumes coincide with the laser focal spot, $R_{\rm pl}(0) = R^*_{\rm pl}(0) = R_{\rm las}$.

Based on the simulation results, we calculate the power and the energy of the absorbed laser radiation as

$$P_{\rm abs} = a_1 n_{\rm e} V_{\rm pl}, \quad E_{\rm abs} = \int P_{\rm abs} dt, \tag{13}$$

the power and the energy of plasma radiation as

$$P_{\rm rad} = \sum_{j=1}^{j_{\max}} b_{6j} E_{\rm ej} V_{\rm pl}, \quad E_{\rm rad} = \frac{1}{2}\int P_{\rm rad} dt, \tag{14}$$

where a factor of 1/2 stands for the radiation into $2\pi$ solid angle. Target EUV emission is characterized by similar quantities—the power and the energy of this EUV radiation are defined as

$$P_{\rm EUV} = \sum_{j=1}^{j_{\max}} A^*_j \theta_j n^*_j E^*_{\rm ej} V_{\rm pl}, \quad E_{\rm EUV} = \frac{1}{2}\int P_{\rm EUV} dt, \tag{15}$$

where

$$E^*_{\rm ej} = \sum_{l\in\{\rm EUV\}} \alpha_{jl} A_{jl} E_{{\rm ej}l} / A^*_j, \quad A^*_j = \sum_{l\in\{\rm EUV\}} \alpha_{jl} A_{jl} \tag{16}$$

are the same sums as in Eq. (8) but are taken only over the lines from the target EUV band. In the present paper, the target band is $11.25 \pm 0.08$ nm in Sec. VI where the comparison to krypton experiments is considered, and $11.2 \pm 0.1$ nm ($\pm 1\%$) in Sec. VII where the EUV light source based on xenon discharge is discussed.

These parameters allow us to calculate key characteristics of the discharge as a source of EUV radiation such as the absorption efficiency (AE) of the laser radiation,

$$\eta_{\rm AE} = E_{\rm abs}/E_{\rm las}, \tag{17}$$

the conversion efficiency (CE) of the laser radiation into the target EUV light

$$\eta_{\rm CE} = E_{\rm EUV}/E_{\rm las}, \tag{18}$$

and the cumulative diameter of the region occupied by the plasma-emitting target EUV radiation,

$$D_{\rm EUV} = \frac{\int 2R_{\rm pl} P_{\rm EUV}\, dt}{\int P_{\rm EUV}\, dt}. \tag{19}$$

The latter quantity characterize the EUV source dimension that may be compared to our experiment in which the discharge is so fast that no time-resolved measurements are possible.

## VI. VALIDATION OF THE MODEL WITH EXPERIMENTAL DATA

Particular values of the cumulative diameter $D_{\rm EUV}$ calculated for the actual parameters of the reported experiments are listed in the last line in Table I. Calculated data demonstrate a fairly good agreement with the measured values. It should be noted here that the agreement has been obtained with a physical model that has almost no free parameters for adjustment. The only possible "degree of freedom," that enters the model but not measured in the experiment, is the neutral gas density before the discharge. We retrieve this value from independent calculations of gas density distribution in a jet flowing from a conical nozzle using the model [39]. The result is a simple link between the initial gas density $n_0$ and the nozzle pressure $p_{\rm nzl}$—the value of $n_0/p_{\rm nzl}$ is approximately constant for the reported conditions,

$$n_0/p_{\rm nzl} \approx 2.7 \times 10^{18}\ {\rm cm^{-3}\ bar^{-1}}. \tag{20}$$

Another neat feature of the discharge that argues in favor of the proposed theory is the transition of the EUV maps from a single maximum distribution at lower pressures to a double maximum distribution at higher pressures, see Fig. 2(c). Such bifurcation occurs at the nozzle pressure about 3 bar. The effect may be related to the initial neutral gas inhomogeneity along the laser beam represented by the $y$ direction.

To illustrate this, we calculate the energy of EUV light within the $11.25 \pm 0.08$-nm wavelength band versus the gas density, see Fig. 3. We see a maximum at $n_0^* = 8 \times 10^{18}$ cm$^{-3}$, which corresponds to the nozzle pressure

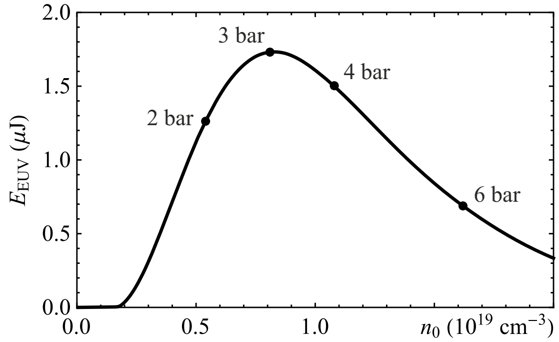


FIG. 3. EUV energy emitted at $11.25 \pm 0.08$ nm by the krypton discharge during one laser pulse as a function of the initial jet density. Points mark the nozzle pressures used in the experiment and presented in Fig. 2.

of 3 bar. The model suggests a physical reason of such maximum. When $n_0 > n_0^*$, the laser energy $E_{\mathrm{abs}}$ absorbed in the discharge increases slower than $n_0$, it even saturates at large densities, so the energy per particle $E_{\mathrm{abs}}/n_0$ decreases. That leads to less krypton ions capable of emitting in the $11.25 \pm 0.08$ nm band ($Kr^{11+}$ and higher). Figure 3 corresponds to the total energy emitted in $4\pi$ while $n_0$ represents the central (maximal) density on the jet axis. However, a similar dependence must characterize a relation between the local value of the initial gas density $n_0(y)$ at point $y$ and the EUV signal $J_{\mathrm{EUV}}(y)$ collected by the microscope from the same point. The reason is that the laser intensity has a relatively flat distribution along $y$ and, except electron-temperature equalizing, there is no mass and energy transport between neighboring $y$ positions during a short laser pulse. Therefore, when $\max n_0(y) < n_0^*$ at pressures below 3 bar, $J_{\mathrm{EUV}}(y)$ has a maximum at $y = 0$; otherwise, $y = 0$ corresponds to a local minimum of $J_{\mathrm{EUV}}(y)$ and there are two maximums located at $n_0(y) = n_0^*$. Some asymmetry in the double maximum regimes observed in the experiment, is related to the longitudinal inhomogeneity of the laser beam due to its absorption.

Thus, the expansion model explains well a spatial structure of the EUV-emitting discharge measured in a dedicated experiment. Similar experiments have been performed in xenon, which also confirms the expansion concept of the EUV-emitting zone. However, due to strong reabsorption of the EUV line radiation in xenon, quantitative interpretation of the measured EUV images is not so clear and straightforward as for the krypton discharge, so we are going to present these results in a separate paper.

As shown earlier [16], the model is able to reproduce key absolute characteristics of the discharge such as EUV light energy values up to 5 mJ at $11.16 \pm 0.13$ nm measured in xenon experiment [12], or absorbed energies of laser beam up to 600 mJ measured in xenon experiments [11]. Dependencies of these characteristics on the gas pressure and laser focus are also in good agreement with the experimental data. Comparison to the experiments gives credit to applying the verified physical model for seeking an optimal regime for a possible high-performance pointlike EUV light source for lithography.

## VII. OPTIMIZED EUV LIGHT SOURCE

To meet common requirements, the EUV light source for high-volume chip manufacturing should have an average power over 100 W and linear dimensions less than 500 $\mu$m [40].

As discussed already, xenon is more preferable for the generation of EUV light than krypton because its better EUV emissivity and more optimal band that fits the characteristic of the available multilayer EUV mirrors. As a good candidate for the discharge driver, we consider the Yb:YAG laser as its radiation (1.030 $\mu$m) may propagate in a dense plasma needed for efficient EUV light generation. The critical electron density is $n_{\mathrm{cr}} \approx 10^{21}$ cm$^{-3}$ at a wavelength of 1 $\mu$m, while the required electron density is about $10^{20}$ cm$^{-3}$ (corresponding to plasma at the atmospheric pressure with an average charge state 10). The collisional absorption length for such plasma is 100 $\mu$m; that is sufficient to support a compact discharge.

Our strategy is to find a maximal CE of a single laser pulse into EUV light in the target band; the average power is then determined by a pulse repetition rate. To increase CE, the pulse duration should be as short as possible to reduce the convective energy losses but long enough to ionize plasma to high charge states required for EUV emission. The focal region should be located at the jet edge so that the EUV light may exit with minimal possible absorption into one of hemispheres, where the collecting mirror is located. The radiation propagating into the second hemisphere and being absorbed inside the jet is spent on expansion of the emitting region. To satisfy the demand of a pointlike source, the focal depth of the laser beam and the radius of the xenon jet are adjusted such that discharge size along the laser beam is close to 500 $\mu$m.

With these constrains, there are three quantities to be tuned: the laser pulse duration, the size of the focal waist, and the nozzle pressure that defines the initial neutral gas density. To find the optimal set, we iterate the expanding discharge model with the goal to maximize CE. Physically this optimum occurs for a particular ion-charge state distribution (from $Xe^{10+}$ to $Xe^{12+}$) corresponding to the maximum EUV emissivity at $11.2 \pm 1\%$ nm.

An example of such optimization is presented in Table III and Fig. 4. Here we fix the parameters proposed for the Alpha-Machine, a project aimed at demonstration of a lithographer based on xenon EUV light source and optics at shorter than 13.5-nm wavelength [17], being currently developed at IPM/IAP RAS. In this machine, a thin-rod

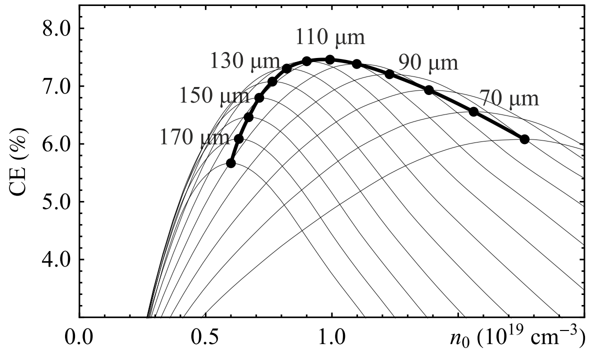


FIG. 4. Maximal EUV conversion efficiency at $11.2 \pm 1\%$ nm in xenon as a function of the initial jet density. Thin lines show CE for particular laser beam waists ($D4\sigma$).

Yb:YAG laser [41,42] generating 60 mJ/few-ns pulses will be focused on a xenon jet with radius up to 1000 μm limited by the ability to pump out of a vacuum chamber. The maximum expected conversion efficiency is 7.5% related to the laser energy delivered to the focal spot—this exceeds a well-known result of CE about 6% reached in the commercial ASML scanners of NXE series based on the Sn-droplet evaporation technology [13].

A good performance of the xenon EUV source may be obtained in a rather broad pressure range, see Fig. 4. This range is limited by poor absorption of laser radiation at low gas densities and its refraction at high densities. EUV light will be collected and transported to an intermediate focus by a single Ru/Be mirror system with 72% reflectivity in the $11.2 \pm 1\%$-nm band [7]. With the planned pulse repetition rate of 1.5 kHz, the average EUV power would be 5 W, which is still below the required level for a mass-production lithographer but suitable for a demo machine. This technical limitation may be overcome by increasing the pulse repetition rate up to 30 kHz, which seems feasible.

TABLE III. Optimization of the xenon EUV light source.

| | |
|---|---|
| Input parameters: | |
| Laser pulse energy/duration | 60 mJ/1.2 ns |
| Laser focal distance (2 × Rayleigh len.) | 500 μm |
| Laser focal waist ($D4\sigma$) | 110 μm |
| Radius of xenon jet | 600 μm |
| On-axis jet gas density | $1.0 \times 10^{19}$ cm$^{-3}$ |
| Calculated discharge characteristics: | |
| Average ion density[a] | $0.7 \times 10^{19}$ cm$^{-3}$ |
| Average electron density | $7.1 \times 10^{19}$ cm$^{-3}$ |
| Average electron temperature | 40 eV |
| Energy balance (% of laser energy per pulse): | |
| Absorbed laser energy | 80% |
| Total radiation losses | 72% |
| EUV radiation at $11.2 \pm 1\%$ nm into $2\pi$ (conversion efficiency) | 7.5% |

[a]Composed of 40% $Xe^{9+}$, 33% $Xe^{10+}$, 23% $Xe^{11+}$, 2% $Xe^{12+}$.

## VIII. CONCLUSIONS

The EUV light source based on a laser discharge in a high-pressure xenon jet has a number of advantages over existing sources based on the laser evaporation of a tin droplet. Dense xenon plasma is formed in the jet that emits EUV light with comparable or even higher power than tin plasma, but the wavelength is shorter, and the focusing optics is not contaminated by the remains of evaporated tin. It is possible to provide a sharp plasma and vacuum boundary using a jet flowing from a conical supersonic nozzle that allows EUV light to pass with minimal absorption in one of the hemispheres while radiation to another hemisphere is used to expand the EUV-emitting region. Besides, Ru/Be optics is characterized by better reflectivity at $11.2 \pm 1\%$ nm than Mo/Si optics at $13.5 \pm 1\%$ nm. An obvious drawback of the presented concept is related to the necessity of using a continuous gas jet for a high-average-power source. In this case, considerably more particles enter the vacuum chamber per unit time compared to the discrete tin droplets used in the usual scheme, which leads to increased requirements for pumping out.

The Alpha-Machine project is proposed as a further development of the concept. At this step, all systems of the 11.2-nm lithographer will be tested, including Ru/Be optics and the xenon EUV light source. The results will provide a basis for an industrial prototype.

## ACKNOWLEDGMENTS

The work was supported by the Russian Science Foundation Grant No. 23-22-00270.

[1] H. Tanuma, H. Ohashi, S. Fujioka, H. Nishimura, A. Sasaki, and K. Nishihara, 4d-4f unresolved transition arrays of xenon and tin ions in charge exchange collisions, J. Phys. Conf. Ser. **58**, 231 (2007).

[2] N. I. Chkhalo and N. N. Salashchenko, Next generation nanolithography based on Ru/Be and Rh/Sr multilayer optics, AIP Adv. **3**, 082130 (2013).

[3] G. D. Kubiak, L. J. Bernardez, and K. D. Krenz, High-power extreme-ultraviolet source based on gas jets, Proc. SPIE **3331**, 81 (1998).

[4] R. H. Moyer, H. Shields, A. Martos, S. W. Fornaca, R. J. St. Pierre, and M. B. Petach, Laser-produced plasma (LPP) scale-up and commercialization, Proc. SPIE **4343**, 249 (2001).

[5] H. Shields, S. W. Fornaca, M. B. Petach, M. Michaelian, R. D. McGregor, R. H. Moyer, and R. J. St. Pierre, Xenon target performance characteristics for laser-produced plasma EUV sources, Proc. SPIE **4688**, 94 (2002).

[6] B. A. M. Hansson, O. Hemberg, H. M. Hertz, M. Berglund, H.-J. Choi, B. Jacobsson, E. Janin, S. Mosesson, L. Rymell,

J. Thoresen, and M. Wilner, Characterization of a liquid-xenon-jet laser-plasma extreme-ultraviolet source, Rev. Sci. Instrum. **75**, 2122 (2004).

[7] R. M. Smertin, N. I. Chkhalo, M. N. Drozdov, S. A. Garakhin, S. Yu. Zuev, V. N. Polkovnikov, N. N. Salashchenko, and P. A. Yunin, Influence of Mo interlayers on the microstructure of layers and reflective characteristics of Ru/Be multilayer mirrors, Opt. Express **30**, 46749 (2022).

[8] A. N. Nechai, A. A. Perekalov, N. N. Salashchenko, and N. I. Chkhalo, Emission spectra of heavy inert gases Kr and Xe in the range from 3 to 20 nm obtained under pulsed laser excitation using various gas jets as targets, Opt. Spectrosc. **129**, 363 (2021).

[9] N. I. Chkhalo, S. A. Garakhin, A. Ya. Lopatin, A. N. Nechay, A. E. Pestov, V. N. Polkovnikov, N. N. Salashchenko, N. N. Tsybin, and S. Yu. Zuev, Conversion efficiency of a laser-plasma source based on a Xe jet in the vicinity of a wavelength of 11 nm, AIP Adv. **8**, 105003 (2018).

[10] S. G. Kalmykov, P. S. Butorin, and M. E. Sasin, Xe laser-plasma EUV radiation source with a wavelength near 11 nm—optimization and conversion efficiency, J. Appl. Phys. **126**, 103301 (2019).

[11] S. G. Kalmykov, P. S. Butorin, M. E. Sasin, and V. S. Zakharov, Absorption of laser radiation in a laser-produced plasma of Xe: Hydrodynamic effects and nonequilibrium ionization, J. Phys. D: Appl. Phys. **55**, 105203 (2022).

[12] V. E. Guseva, A. N. Nechay, A. A. Perekalov, N. N. Salashchenko, and N. I. Chkhalo, Investigation of emission spectra of plasma generated by laser pulses on Xe gas-jet targets, Appl. Phys. B **129**, 155 (2023).

[13] J. van Schoot, Exposure tool development toward advanced EUV lithography: A journey of 40 years driving Moore's law, IEEE Trans. Electron Devices **2**, 8 (2024).

[14] I. Fomenkov, A. Schafgans, and D. Brandt, Laser-produced plasma sources for high-volume-manufacturing EUV lithography, Synchrotron Radiat. News **32**, 3 (2019).

[15] M. Purvis, I. V. Fomenkov, A. A. Schafgans, M. Vargas, S. Rich, Y. Tao, S. I. Rokitski, M. Mulder, E. Buurman, M. Kats *et al.*, Industrialization of a robust EUV source for high-volume manufacturing and power scaling beyond 250W, Proc. SPIE **10583**, 1058327 (2018).

[16] I. S. Abramov, S. V. Golubev, E. D. Gospodchikov, and A. G. Shalashov, Expansion of laser discharge in xenon jet improves EUV-light emission, Appl. Phys. Lett. **123**, 193502 (2023).

[17] N. I. Chkhalo, New concept for the development of high-performance $X$-ray lithography, Russ. Microelectron. **53**, 397 (2024).

[18] J. A. R. Samson and W. C. Stolte, Precision measurements of the total photoionization cross-sections of He, Ne, Ar, Kr, and Xe, J. Electron Spectros. Relat. Phenomena **123**, 265 (2002).

[19] J. B. West and G. V. Marr, The absolute photoionization cross sections of helium, neon, argon and krypton in the extreme vacuum ultraviolet region of spectrum, Proc. R. Soc. Lond. A **349**, 397 (1976).

[20] S. Yu. Zuev, A. Ya. Lopatin, V. I. Luchin, N. N. Salashchenko, D. A. Tatarskiy, N. N. Tsybin, and N. I. Chkhalo, Comparative study of the thermal stability of Be-based extreme ultraviolet pellicles, Tech. Phys. **68**, S630 (2023).

[21] M. V. Svechnikov, N. I. Chkhalo, S. A. Gusev, A. N. Nechay, D. E. Pariev, A. E. Pestov, V. N. Polkovnikov, D. A. Tatarskiy, N. N. Salashchenko, F. Schäfers *et al.*, Influence of barrier interlayers on the performance of Mo/Be multilayer mirrors for next-generation EUV lithography, Opt. Express **26**, 33718 (2018).

[22] T. Harada, N. Teranishi, T. Watanabe, Q. Zhou, J. Bogaerts, and X. Wang, High-exposure-durability, high-quantum-efficiency ($>$ 90%) backside-illuminated soft-$X$-ray CMOS sensor, Appl. Phys. Express **13**, 016502 (2020).

[23] Yu. P. Raizer, *Gas Discharge Physics* (Springer-Verlag Berlin, Heidelberg, 1991).

[24] V. M. Povyshev, A. A. Sadovoy, V. P. Shevelko, G. D. Shirkov, E. G. Vasina, and V. V. Vatulin, Electron-impact ionization cross sections of H, He, N, O, Ar, Xe, Au, Pb atoms and their ions in the electron energy range from threshold up to 200 keV, JINR Commun. No. E9-2001-148 (2001).

[25] A. V. Philippov, V. M. Povyshev, A. A. Sadovoy, V. P. Shevelko, G. D. Shirkov, E. G. Vasina, and V. V. Vatulin, Electron-impact ionization cross sections of Ti, Kr, Sn, Ta, U atoms and their ions in the electron energy range from the threshold up to 200 keV, JINR Commun. No. E9-2002-5 (2002).

[26] Ya. B. Zeldovich and Yu. P. Raizer, *Physics of Shock Waves and High-Temperature Hydrodynamic Phenomena* (Academic Press, NY, 1966).

[27] S. S. Churilov, Y. N. Joshi, J. Reader, and R. R. Kildiyarova, $4p^64d^8 - (4d^75p + 4d^74f + 4p^54d^9)$ transitions in Xe XI, Phys. Scr. **70**, 126 (2004).

[28] S. S. Churilov and Y. N. Joshi, Analysis of the $4p^64d^84f$ and $4p^54d^{10}$ configurations of Xe X and some highly excited levels of Xe VIII and Xe IX ions, Phys. Scr. **65**, 40 (2002).

[29] R. D. Cowan, *The Theory of Atomic Structure and Spectra* (University of California Press, Berkeley, 1981).

[30] H. Van Regemorter, Rate of collisional excitation in stellar atmospheres, Astrophys. J. **136**, 906 (1962).

[31] D. H. Sampson and H. L. Zhang, Use of the Van Regemorter formula for collision strengths or cross-sections, Phys. Rev. A **45**, 1556 (1992).

[32] I. S. Abramov, E. D. Gospodchikov, and A. G. Shalashov, Extreme-ultraviolet light source for lithography based on an expanding jet of dense xenon plasma supported by microwaves, Phys. Rev. Appl. **10**, 034065 (2018).

[33] J. P. Apruzese, An analytic Voigt profile escape probability approximation, JQSRT **34**, 447 (1985).

[34] S. Fujioka, H. Nishimura, K. Nishihara, A. Sasaki, A. Sunahara, T. Okuno, N. Ueda, T. Ando, Y. Tao, Y. Shimada *et al.*, Opacity effect on extreme ultraviolet radiation from laser-produced tin plasmas, Phys. Rev. Lett. **95**, 235004 (2005).

[35] E. R. Kieft, K. Garloff, J. J. A. M. van der Mullen, and V. Banine, Comparison of experimental and simulated extreme ultraviolet spectra of xenon and tin discharges, Phys. Rev. E **71**, 036402 (2005).

[36] L. Spitzer and R. Harm, Transport phenomena in a completely ionized gas, Phys. Rev. **89**, 977 (1953).

[37] S. I. Braginskii, Transport phenomena in a completely ionized two-temperature plasma, Sov. Phys. JETP **6**, 358 (1958).

[38] S. I. Braginskii, Transport processes in a plasma, Rev. Plasma Phys. **1**, 205 (1965).

[39] M. A. Korepanov, M. R. Koroleva, and E. A. Mitrukova, Numerical investigation of flows with condensation in micronozzles, J. Phys.: Conf. Ser. **2057**, 012016 (2021).

[40] V. Bakshi, *EUV Sources for Lithography* (SPIE Press, Bellingham, Washington, 2006).

[41] I. Kuznetsov, I. Mukhin, O. Palashov, and K. Ueda, Thin-tapered-rod Yb:YAG laser amplifier, Opt. Lett. **41**, 5361 (2016).

[42] I. Kuznetsov, S. Chizhov, and O. Palashov, Yb:YAG diverging beam amplifier with 20 mJ pulse energy and 1.5 kHz repetition rate, Opt. Lett. **48**, 1292 (2023).